EuroSun2026

CROSS-SEASONAL STUDY OF INDIRECT WATER-IN-GLASS INTEGRATED STORAGE SOLAR COLLECTORS IN OPERATIONAL CONDITIONS

Mehdi Salah [1,2] (*), Hervé Noël [1], Diane Le Roux [1], Adrien Fuentes [1], Anthony Magueresse [1], Liqun Feng [2], Thibaut Colinart [1]

[1] IRDL, UMR CNRS 6027, Univ. Bretagne Sud, Bretagne INP, ENSTA, Institut Polytechnique de Paris, Univ. Brest, Lorient, France.

[2] Feng Technologies SAS, Entrammes, France

(*) corresponding author: mehdi.salah@univ-ubs.fr

Summary

This study presents an experimental and numerical analysis of water-in-glass evacuated tube solar collectors (WiG-ETC) with integrated storage and internal heat exchanger. The solar thermal installation is located in northwest France and is used for heating a livestock farm building. It was instrumented and then monitored for two years. In parallel, a model was developed using TRNSYS to simulate temperatures at different points in the solar field and recovered thermal energy. Four representative experimental data sequences in April, July, September and February were selected to conduct model calibration. A Morris sensitivity analysis was performed on an initial set of 10 parameters related to the ETC, integrated storage, heat exchanger and the environment. A subset of 6 parameters was retained for identification. It was conducted through mono-objective optimization using Powell algorithm. The calibration process was repeated on the four sequences and results are compared. The calibrated seasonal model simulations showed good agreement with the reference data with a relative error of 0.34%, -0.14%, -2.94% and -3.15% respectively, on total useful solar energy production, and a mean average percentage error between 4.58% and 6.01% for integrated storage simulated temperature.

Keywords: Evacuated tube collector, Internal heat exchanger, TRNSYS, Sensitivity analysis, Model calibration

Field of application for the findings: Solar thermal systems design and characterization

Addressed audience: Researchers and Engineers

---

1. Introduction

The Evacuated Tube Collector (ETC) is a mature solar thermal technology. Their share among low temperature solar thermal collectors is significant: in 2023, ETCs represented 61% of newly installed collectors in the world (AEE - INTEC, 2025). This trend can be linked to the good performance of ETCs: experimental studies report collector efficiencies ranging from 45.3% (Siuta-Olcha *et al.*, 2021) up to 60% (Hayek *et al.*, 2011), depending on the ETC variant and location. This performance advantage is particularly notable for ETCs operating in mid-latitude European climates with low irradiance (Ayompe *et al.*, 2011; Zambolin and Del Col, 2010). Two design features explain this: a vacuum around the absorber surface limits convective losses and allows higher operating temperatures (N'Tsoukpoe *et al.*, 2026), while the tubular geometry reduces optical losses at non-normal solar incidence angles (Rahimi-Ahar *et al.*, 2023).

Among ETC technologies, Water-in-Glass (WiG) tubes, are a simple and reliable design used in the industry (Morrison *et al.*, 2004). They operate through natural convection – thermosiphon effect – which makes it possible to combine solar collection and thermal storage within a single unit (Smyth *et al.*, 2006). This design is known as Integrated Collector-Storage (ICS) units, where the open ends of the WiG tubes are directly connected to a horizontal, low-pressure storage tank.

In the case where a single fluid is used as both the storage medium and the Heat Transfer Fluid (HTF), the assembly is called direct WiG-ICS. Several studies have addressed direct WiG-ICS modeling, using two main approaches: analytical and dynamic. Singh *et al.* (2023) proposed a simplified analytical model based on energy balances, to predict the outlet temperature of two WiG-ICS units in series. The model was validated over a two-day period. Root Mean Square Errors (RMSE) for temperature was less than 0.85°C. However, their model was based on assumptions of constant tank outlet temperature and flowrate. Therefore, it was not suitable for long-term predictions under variable conditions. Dynamic modeling allows long-term, multi-parameter simulation. It is commonly implemented on simulation software such as TRNSYS, where predefined components for conventional solar thermal systems are available. However, no such component exists for WiG-ICS units. To address this need, Budihardjo *et al.* (2007) worked on modeling direct WiG-ICS units using pre-existent TRNSYS components. An empirical correlation for the Reynolds number was used to implement the thermosiphon flow. This equation was established using measured temperatures and flowrates at the tube ends, along with the corresponding CFD results under different irradiance conditions. In a following work, this modeling approach was used in a TRNSYS simulation of two direct WiG-ICS models under Sydney climate. Annual results showed solar fractions between 57.5% and 71% (Budihardjo and Morrison, 2009).

Later studies extended this TRNSYS framework to compound direct WiG-ICS installations. Ahmadreza Mohammadkarim *et al.* (2014) studied a domestic hot water system with a 2 m² direct WiG-ICS unit, and a vertical storage tank with auxiliary heater. Simulations covered two representative days, one in summer and one in winter, under the Tehran climate. The model results for simulated collector efficiencies were between 50% and 60%, which matched experimental results in the literature. A numerical study conducted by Gambade *et al.* (2023) applied the same modeling approach to 16 direct WiG-ICS units in northwest France over a longer period. Beside installation modeling, their work involved the model calibration using a 12-day experimental sequence with varied weather conditions. This allowed them to estimate the collector optical and thermal efficiencies, as well as the integrated storage heat loss coefficient. The calibrated model was then validated over a 5-month period. The simulated solar production was accurately estimated with a Percentage Error (PE) of -0.2% and a Mean Absolute Percentage Error (MAPE) of 8.5%.

Direct WiG-ICS systems offer a good compromise between cost, efficiency, and reliability across climates. However, their use is limited to low-pressure setups for hot water production (Rahimi-Ahar *et al*., 2023). The indirect WiG-ICS design addresses this limit. It uses a submerged Heat Exchanger (HEX) inside the storage tank. This separates two fluids: HTF and Stagnant Solar Water (SSW). The HTF circulates inside the HEX, driven by a pump, while the SSW surrounds the submerged HEX and circulates passively between the tank and the tubes. Heat transfer from the SSW to the HTF allows heat extraction from each unit. Also, units can be linked in series through their HEX. As a result, scalable installations of multiple indirect WiG-ICS units can be used for pressurized closed loop such as building heating or district heating networks.

In general, studies involving ICS units with submerged HEX are scarce in the literature. Koffi *et al.* (2008) studied a Flat Plate Collector ICS unit with a 6-meter submerged coiled-tube HEX. It was experimentally characterized under Ivory Coast conditions. Their results highlighted an enhanced collector efficiency up to 68.3% on sunny days and an average HEX heat transfer coefficient of 149 W/m².K^{-1}. Other sources conducted experimental studies focused on experimental performance evaluation using alternative HTFs, such as R22 refrigerant (Pluta and Pomierny, 1995) or copper-oxide nanofluid (Ghaderian *et al*., 2017). This latter work used a WiG-ICS unit with a parabolic concentrator, but results were not targeted towards collector characterization. Sadeghi *et al.* (2020) used a similar approach to study a WiG-ICS collector efficiency, varying the nanofluid volume fraction and the fluid flowrate. The three AI-driven numerical methods were compared to predict efficiency and the inlet-outlet temperature. These studies confirm the enhanced performances of submerged-HEX for ICS systems in general. However, proper experimental or numerical characterization of indirect WiG-ICS units are, to the best of our knowledge, inexistent in the literature.

This study focuses on the dynamic modeling and characterization of an indirect WiG-ICS experimental installation. The objective is to calibrate the model through sensitivity analysis and parameter identification, using a variety of seasonal experimental data. The solar installation is used to heat a livestock building. The HTF circulation profiles are intermittent due to variations in heating demand and available stored sensible energy. These particular operational conditions, along with the constraints imposed by the submerged coiled-tube HEX, make it interesting to study how the model parameters' effects and values react to these elements.

2. Methodology

2.1. Experimental Setup

The investigated solar thermal installation is made with indirect WiG-ICS system (FENGTECH® ETF-2) (see Fig.1). The system is composed of 30 WiG tubes plugged into the lower part of a 240 L SSW horizontal storage tank (insulated with 60-mm layer of polyurethane). The horizontal storage tank of the unit contains a coiled-tube stainless steel HEX (length: 15 m; coil diameter: 320 mm; coil pitch: 150 mm).

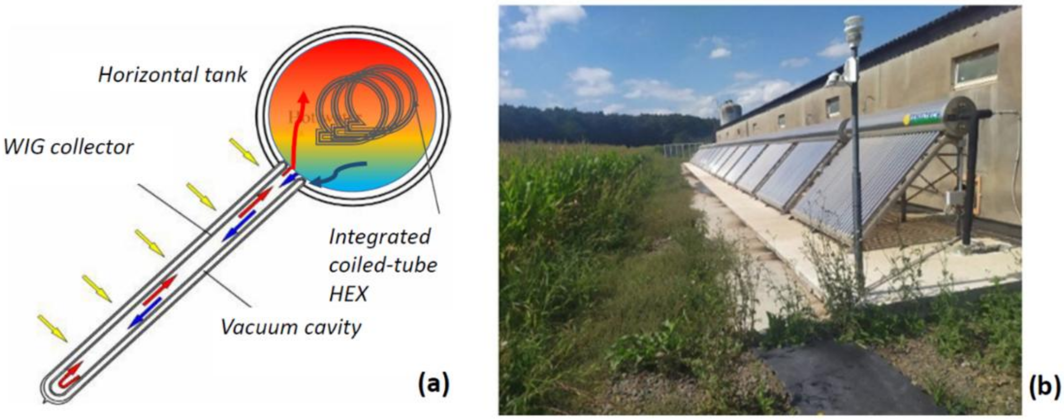

Fig.1: (a) Schematic cross-section of the studied WiG-ICS unit - (b) Photo of the investigated solar thermal installation.

The experimental site is located in northwest France [47°11'11"N, 0°43'00"W]. The installation consists of 14 WiG-ICS units, south-oriented with a tilt angle of 45°. The total ETC gross area is 54.2 m^2, paired with a 3.1 m^3 SSW storage volume. The WiG-ISC units are linked in series via their integrated HEX. Within a 83-meter closed loop, the solar field pump drives HTF at a constant flowrate of 800 $L \cdot h^{-1}$. The solar installation is coupled with a 1000-Liter buffer tank located in the boiler room. The buffer tank temperature is kept within a 45–60 °C operating range by a 55 kW auxiliary propane condensing boiler. HTF circulation is activated once temperature difference between SSW of last tank and hot water storage is higher than 4 °C.

The installation is fitted with on-site measurement sensors and a data logging system. The solar field relevant instrumentation is detailed in Tab.1. A weather station, positioned near the collectors with a clear southern horizon, records on-site weather data. All data is logged online since March 2024 with a times-step of 300 s.

Tab.1: Solar field instrumentation inventory.

Instrument	Number deployed	Measures (Number)	Uncertainty
PT1000 sensors	14	SSW temperature in units 1,3,5,7,9,11,13,14 tanks (12) Solar HTF temperatures at buffer tank inlet and outlet (2)	±0.5 °C
Flow meter	1	Solar HTF flowrate	±1%
Pyranometer	1	Global Horizontal Irradiance G_h	±3%
Pulse meter	1	Auxiliary boiler propane volume	±1%
Weather station	1	Ambient temperature, relative humidity, wind speed	–

2.2. Numerical Model

The set-up is modeled on TRNSYS 18 software. The indirect WiG-ISC is modeled as a multi-component assembly of a selection of predefined Types, as shown in the Fig.2.

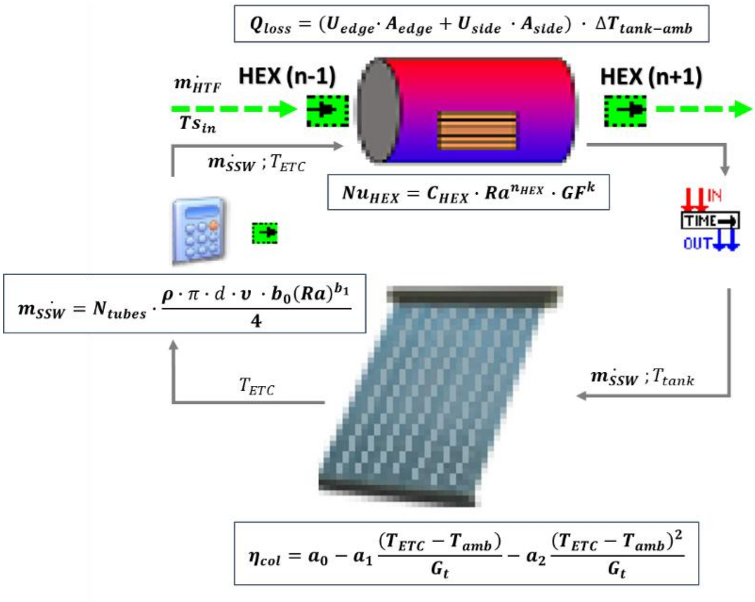

Fig.2: TRNSYS model of indirect WiG-ETC Unit: main equations and data flow.

Type 71 is used to model an ETC module with quadratic efficiency. It takes as input the Global Titled Irradiance G_T, the ambient temperature T_{amb} and an inlet fluid temperature and flowrate. As output, it computes an average outlet SSW temperature T_{ETC} ascending to the horizontal storage tank. The ETC efficiency η_{col} is characterized by the coefficients' optical efficiency a_0 (-), linear thermal efficiency a_1 ($W.m^{-2}.K^{-1}$), and quadratic thermal efficiency a_2 ($W.m^{-2}.K^{-2}$).

$$\eta_{col} = a_0 - a_1 \frac{(T_{ETC}-T_{amb})}{G_T} - a_2 \frac{(T_{ETC}-T_{amb})^2}{G_T} \quad \text{(eq. 1)}$$

An equation module is used to compute the thermosiphon mass flow rate of the SSW, using the empirical correlation of Budiharjdo *et al.* (2007) for the flow exiting a single ETC tube. This correlation takes into account the tube diameter d, the SSW density and the dynamic viscosity (ρ, υ) as:

$$\dot{m}_{SSW} = N_{tubes} \frac{\rho \cdot \pi \cdot d \cdot \upsilon \cdot b_0 (Ra)^{b_1}}{4} \quad \text{(eq. 2)}$$

Ra (-) is Rayleigh numbers for SSW in the ETC tubes and b0 and b1 are dimensionless coefficients. During nighttime, a simplifying assumption is to set reverse thermosiphon mass flowrate to 0 (Tang and Yang, 2014).

Type 1533 models the horizontal cylindrical storage tank with an internal HEX. The SSW enters and exits the tank through defined inlet and outlet nodes. These nodes were set at mid-height of the horizontal tank (Dileep *et al.*, 2020). The nodal discretization of the HEX length and tank volume, and their coupling, were set following the adjustments discussed in the literature (Unrau, 2017). The heat transfer between SSW and the internal coiled-tube HEX is characterized by Nusselt number:

$$Nu_{HEX} = C_{HEX} \cdot Ra^{n_{HEX}} \cdot GF^k \quad \text{(eq. 3)}$$

where Ra (-) is Rayleigh number for SSW inside the tank, GF (-) is a geometrical view factor, and C_{HEX} (-), n_{HEX} (-) and k (-) are empirical dimensionless parameters. Type 1533 also computes convective heat loss Q_{loss} through its lateral surface (A_{edge}) and vertical walls surface (A_{side}), and the ambient to internal temperature difference $\Delta T_{tank-amb}$. U_{edge} and U_{side} are the corresponding heat loss coefficients ($W.m^{-2}.K^{-1}$).

$$Q_{loss} = (U_{edge} \cdot A_{edge} + U_{side} \cdot A_{side}) \cdot \Delta T_{tank-amb} \quad \text{(eq. 4)}$$

Finally, thermal balance between the integrated storage tank and the solar collector is achieved by Type 150. It ensures temperatures and flowrates convergence at each time step.

The global model is created by linking consecutive HEX temperature and flowrate outlets of Type 1533 of the 14 WiG-ICS. Supply and return pipes of solar field to the buffer tank are modeled using Type 952a (buried pipe) and Type 31 (aerial pipe). As input, the global model uses G_h, ambient temperature T_{amb}, HTF volumetric flowrate Qv_s and HTF solar field inlet temperature $T_{s\,in}$. The crude irradiance measurements are filtered for cloud-enhanced values (Gueymard, 2017) and transposed to G_T by Type 16c.

The final model outputs are, among others, SSW temperatures in tanks 1, 7 and 14 and temperature at the outlet of the solar thermal installation $T_{s\,out}$. From these data, the simulated daily (E_s^d) and total (E_s^T) useful solar thermal energy are calculated as follows:

$$E_s = \int Qv_s \cdot \rho \cdot c_p \cdot (T_{s\,out} - T_{s\,in}) \cdot dt \qquad \text{(eq. 5)}$$

2.3. Model Calibration

A global sensitivity analysis is carried on the model to identify the most influential parameters. An initial set of 10 parameters is defined (see Tab.2). The Morris one-at-a-time is used to assess the elementary effects of each parameter in the set. It computes through two summary indices: the mean of absolute effects μ^*, and the standard deviation σ. The final subset of the most influential parameters is selected based on the $\frac{\mu*}{\max(\mu*)}$ ratio (Saltelli, 2002). The ratio $\frac{\sigma}{\mu*}$ helps to determine the linearity and monotony of the effect of each parameter (Garcia Sanchez *et al.*, 2014). The Morris One-at-A-Time method is applied using Python's SALib library (Herman and Usher, 2017) coupled to the TRNSYS model.

Tab.2: Parameters investigated in the sensitivity analysis.

Parameter	Unit	Reference value	Sampling interval
a_0	-	0.75	[0.5 - 0.85]
a_1	$W.m^{-2}.K^{-1}$	1.29	[0.83 - 1.94]
b_1	-	0.1914	[0.18 - 0.21]
b_0	-	0.4048	[0.40 - 0.42]
U_{side}	$W.m^{-2}.K^{-1}$	0.412	[0.288 – 0.536]
U_{edge}	$W.m^{-2}.K^{-1}$	0.441	[0.309 – 0.575]
Albedo	-	0.2	[0.1 - 0.8]
C_{HEX}	-	0.6	[0.3 - 0.9]
n_{HEX}	-	0.25	[0.18 - 0.33]
GF	-	0.5	[0.9 - 1.2]

The sampling intervals for a_0, a_1, b_0, b_1 are defined similarly to related works (Gambade *et al.*, 2023). The parameter a_2 (quadratic thermal efficiency) was not considered for the analysis because its effect is physically limited when the collectors operate at relatively low temperatures (less than 100 °C) (Chamsa-ard *et al.*, 2014). For the remaining parameters, the interval boundaries are set at ± 30% around the reference value. These values are either derived from system thermo-physical properties (U_{side} = 0.412 $W.m^{-2}.K^{-1}$; U_{edge} = 0.441 $W.m^{-2}.K^{-1}$) or taken from TRNSYS default settings.

Once identified, the values of most influential parameters are estimated to calibrate the TRNSYS global model. The calibration is performed on daily useful solar thermal energy E_s^d. To limit the amplification effect of low-production days on the simulation errors (Yang *et al.*, 2023), a Weighted Mean Average Percentage Error (WMAPE) is used as the objective function, where the deviation simulated daily energy production E_{sim}^d is referenced to the maximum daily experimental energy production E_{exp}^d over the sequence N_d days considered.

$$WMAPE_{max} = \frac{1}{N_d} \cdot \sum_d \frac{\left|E_{exp}^d - E_{sim}^d\right|}{max(E_{exp}^d)} \qquad \text{(eq. 6)}$$

The optimization is implemented through the Python Pymoo library (Blank and Deb, 2020), through a coupled

Python-TRNSYS interface. Powell algorithm (Powell, 1964) is applied on the parameter space over 300 iterations.

3. Results and Discussion

3.1. Experimental data sequences

Four experimental sequences, spanning the four seasons of 2024, were selected to characterize the system's performance under a wide range of operating conditions.

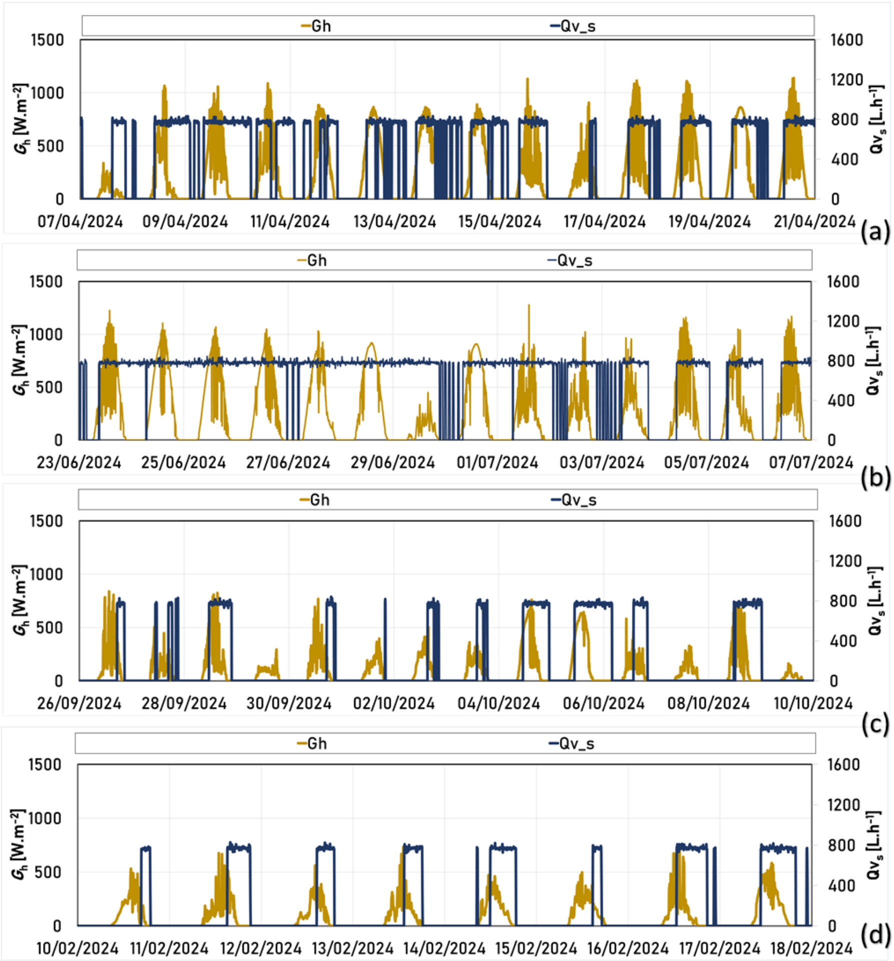

Fig.3: Selected Qv_s and G_h experimental data for model calibration across the seasons in 2024: (a) spring, (b) summer, (c) autumn, (d) winter.

The four periods show different combinations of irradiation amplitude and flowrate continuity. The first three selected sequences (see Fig.3a, 3b, 3c) are two-week periods with comparable data volume. The last sequence (see Fig.3d) for winter conditions is limited to 8 days to the limited periods with active solar pump in that season. For each of the four sequences, a Morris sensitivity analysis is conducted followed by calibration against the corresponding measured useful energy output.

3.2. Experimental data analysis

Tab.3 shows the summary metrics for the experimental conditions and thermal output of the four sequences. Mean ambient temperature and daily irradiation shows normal seasonal tendencies, with highest values in summer (19.15 °C, 20.16 MJ.m^{-2}.day^{-1}), followed by spring, autumn, and winter for the lowest (10.60 °C, 6.62 MJ.m^{-2}.day^{-1}). Pump activation time shows a clear relation with available irradiation. It follows the same tendency and drops from 83.6% in summer to about 23% in autumn and winter.

Tab.3 Solar field experimental data analysis for four seasonal sequences.

	Spring	**Summer**	**Autumn**	**Winter**
Mean daily ambient temperature T_{amb} [°C]	12.19	19.15	13.27	10.60
Mean daily irradiation [MJ/m²/day]	17.60	20.16	7.56	6.62
Pump activation [hours]	205.42	280.92	76.83	45.17
Pump activation [% of period]	57.18	83.59	22.87	23.52
Mean solar field inlet temperature $T_{s\ in}$ [°C]	34.14	45.43	26.69	26.42
Total useful solar thermal energy (E_s^T) [MJ]	5252.08	4476.53	1449.43	511.16

Useful solar thermal energy follows the same trend for summer, autumn and winter. It is noteworthy that the total useful solar thermal production in spring (5252.08 MJ) are higher than that in summer (4476.53 MJ), despite 13% less irradiance and 27% fewer pump operating hours. This is explained by the higher heating demand in spring which shows indirectly in the average HTF return temperature to the solar field $T_{s\ in}$. As the building heating demand is higher due to the weather (T_{amb} = 12.19 °C in spring vs. 19.15 °C in summer), the return temperature is consequently 11 °C lower in spring (34.14 °C vs. 45.43 °C). A lower inlet temperature raises collector efficiency (see eq .1) resulting in higher production.

3.3. Sensitivity analysis

Fig.4 displays the Morris elementary effect matrices for the initial 10 parameters over the 4 sequences. Across all seasons, the same four parameters — a_0, a1, U_{edge}, and Albedo — have the main dominant influences, with the highest μ* values in every plot. Independently of the season, a_0 position on the matrix is always below the σ/μ* = 0.1 line, which indicate a linear stable effect across seasons. The effects of a_1, U_{edge}, and Albedo are slightly less stable across seasons, but it remains in the region of σ/μ* = 0.1 to σ/μ* = 0.5. Their influence is linear but non-monotonic. The HEX related parameters consistently show moderate μ* values. C_{HEX} and n_{HEX} (more specifically) show high σ and sit close to the σ/μ* = 1 line in all four matrices, indicating a strongly nonlinear or interaction-dominated effect. Therefore, their influence is unstable. The remaining parameters b_0, U_{side} and GF have a negligible influence. They cluster near the origin with low μ* and σ in all four seasons. In summary, the elementary effect matrices highlight their main clusters across seasons:

- a stable dominant linear group (a_0, a_1, U_{edge}, and Albedo),
- an unstable high-variance group (b_1, C_{HEX} and n_{HEX}),
- a stable negligible group (b_0, U_{side} and GF).

The $\frac{\mu*}{\max(\mu*)}$ ratios for the 10 parameters in all seasons are displayed in Tab.4. Overall, a_0 is consistently the dominant parameter ($\frac{\mu*}{\max(\mu*)}$ = 1) across all seasons. It is followed by a_1 ($\frac{\mu*}{\max(\mu*)}$ > 0.5), Albedo, and U_{edge}. While Albedo displays stable ratio values (around 0.2) across seasons, a_1 and U_{edge} influences are visibly season-dependent: the lowest values of their ratios are recorded in summer (0.503 for a_1, 0.069 for U_{edge}) and spring. However, their effect is almost doubled in autumn and especially winter (0.852 for a_1, 0.192 for U_{edge}).

The parameters a_1 and U_{edge} represent heat loss coefficients of ETC and the integrated storage, respectively. In the colder seasons, the temperature difference between the SSW and the environment is more significant. Therefore, the heat loss through tank and ETC walls, and the effect of a_1 and U_{edge}, are more pronounced. C_{HEX} and GF do not show clear seasonal dependence. n_{HEX} displays an increased effect in autumn and winter, but given its non-linear nature and possible interactions, this tendency cannot be clearly interpreted.

The final selection of the most influential parameters is based on the average ratio for all seasons. Four parameters – a_0, a_1, U_{edge}, and Albedo – are retained because their average $\frac{\mu*}{\max(\mu*)}$ is above 0.1. It was also decided to retain

C_{HEX} and n_{HEX} for identification, for the purpose of HEX characterization.

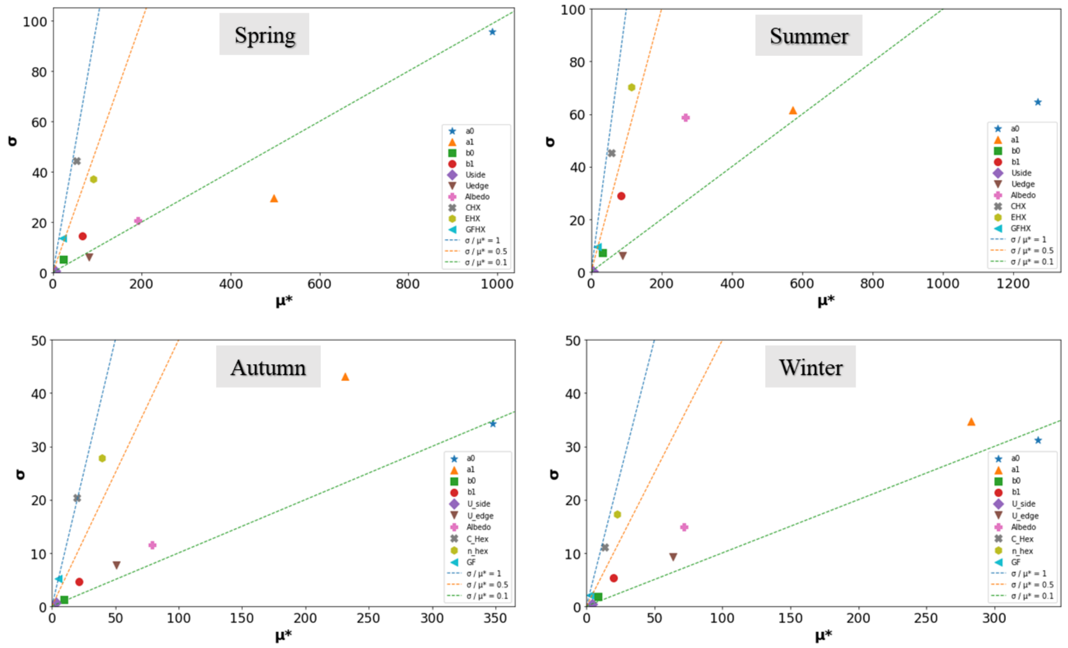

Fig.4: Morris elementary effects matrices for four seasonal sequences.

Tab4. Seasonal normalized values of the mean of absolute effect $\mu *$ ($\frac{\mu *}{\max(\mu *)}$ ratio).

Parameter	**Spring**	**Summer**	**Autumn**	**Winter**	**Average**
a_0	1.000	1.000	1.000	1.000	1.000
a_1	0.503	0.451	0.665	0.852	0.618
b_0	0.023	0.026	0.027	0.026	0.026
b_1	0.067	0.067	0.062	0.060	0.064
U_{side}	0.005	0.005	0.009	0.013	0.008
U_{edge}	0.083	0.069	0.147	0.192	0.123
Albedo	0.194	0.212	0.227	0.217	0.213
C_{HEX}	0.054	0.045	0.056	0.040	0.049
n_{HEX}	0.092	0.091	0.113	0.067	0.091
GF	0.022	0.013	0.014	0.008	0.014

3.4. Model calibration

Tab.5. presents the objective function and errors of the calibrated model across the four seasons. Powell optimization across the four sequences converges to acceptable WAPE values (< 7.5%). The calibrated model shows good agreement with the experimental results for the total useful solar energy simulation, with relative errors between 0.34% and −3.15%. For the tanks SSW temperature, the calibrated model reproduced the average temperature in tank 7 (mid-serie) with good accuracy: the MAPE was less than 5% in spring and summer, and around 6% in winter and autumn.

Tab 5.: Objective function and calibrated model simulated energy and tank temperature errors for the 4 sequences.

	Spring	**Summer**	**Autumn**	**Winter**
WAPE [%]	4.06	6.91	7.11	7.34
PE [%] total energy	0.34	-0.14	-2.94	-3.15
MAPE [%] T_{tank}	4.58	4.68	6.01	5.94

The results of the retained parameters identification across all sequences are displayed in Tab.6. Most parameters estimated values show seasonal variations. It should be noted that, since the calibration is carried out in intermittent operational conditions, these variations should be interpreted as the reaction of the model itself to the input solicitations and the optimization algorithm. This should not be confused with variations of the physical properties of the indirect WiG-ICS.

Tab.6.: Estimated values of the retained 6 parameters for the four sequences.

	Spring	**Summer**	**Autumn**	**Winter**
a_0 [-]	0.67	0.63	0.72	0.79
a_1 [$W \cdot m^{-2} \cdot K^{-1}$]	1.39	1.93	1.45	1.43
U_{edge} [$W \cdot m^{-2} \cdot K^{-1}$]	0.44	0.56	0.57	0.44
Albedo [-]	0.32	0.32	0.50	0.42
C_{HEX} [-]	0.86	0.86	0.89	0.30
n_{HEX} [-]	0.27	0.27	0.32	0.21

The most marked seasonal influence is visible on a_0, a_1. Their variation trends are examined against the experimental season data metrics displayed in Tab.2. It was observed that a_0 shows a clear correlation to the average daily irradiation values (r = - 0.93). This is clearly reflected by its identified value, which is highest in winter (0.79), and lowest in summer (0.63). a_1 shows opposite seasonal tendencies: values are highest in summer (1.93 $W. m^{-2}. K^{-1}$) and lowest in spring (1.39 $W. m^{-2}. K^{-1}$). A strong positive correlation with average ambient temperature (r=0.96) is observed. Overall, these seasonal tendencies for both a_0 and a_1 are coherent with the nature of the parameters. However, an inter-compensation pattern is also observed between the two parameters, with r values between 0.83 and 0.98 across the four sequences. This trade-off is a numerical effect that results from the optimization process: as shown by the sensitivity analysis results (see Tab.4), a_0 and a_1 have the strongest influences on the model output. Therefore, to stabilize the model output around an objective-function minimum, a change in a_0 can be partly compensated by a_1.

In reference, the closest calibration work in the literature was conducted on a direct WiG-ICS operated for farming hot water supply in northwest France (Gambade *et al*., 2023). The installation operation mode is different, where complete voiding of SSW was carried out twice a day. The estimated values, a_0 = 0.75 and a_1 = 1.29 $W. m^{-2}. K^{-1}$ were obtained following a 13-days mixed conditions calibration sequence in September 2022. The results obtained in this work for autumn conditions are very close, which gives confidence in the estimated values.

For the physical characterization of the collector, the retained values are a_0 = 0.63 and a_1 = 1.93 $W \cdot m^{-2} \cdot K^{-1}$, which were obtained with the summer calibration. The summer sequence conditions (high irradiation, stable and continuous HTF flowrate) are the closest to the conditions for standardized thermal performance testing (ISO, 2025) among the sequences.

4. Conclusions

This work presented a numerical characterization study of indirect WiG integrated-storage collector under operational conditions. The installation is located in north-west France and contributes to the heating of a livestock building. A TRNSYS model of the unit was developed by assembling predefined Types for an ETC and a horizontal storage tank with submerged coiled-tube HEX.

An inter-seasonal calibration was carried out using experimental measurements from onsite instrumentation. Four experimental sequences were considered: spring (15 days), summer (14 days), autumn (14 days), and winter (8 days) of the year 2024. The selection of these data sets is intended to illustrate seasonal fluctuations and evolving operating conditions.

A Morris sensitivity analysis was performed on the model of the global installation for the four sequences. Four dominant parameters, valid for all seasons, were selected: the optical efficiency (a_0), the linear thermal loss coefficient (a_1), the tank lateral wall heat loss coefficient (U_{edge}), and the albedo. Two additional parameters related to the HEX were retained to characterize its heat transfer. The selected parameters were identified using a mono-objective Powell optimization. Good agreement was obtained with experimental data regarding total useful solar energy production (relative error ranging from 0.34% to -3.15%) and average integrated storage temperature (MAPE error ranging from 4.58% to 6.01%) across the four sequences.

The seasonal analysis of the calibrated parameters shows that a_0 is strongly correlated with average daily irradiation, and a_1 with ambient temperature. A numerical inter-compensation effect between a_0 and a_1 was also observed. The identified values of a_0 and a_1 for autumn were close to those reported in the literature for a direct WiG-ICS system operating in the same region. Due to its stable conditions, the summer sequence is selected as the reference case ($a_0 = 0.63$, $a_1 = 1.93$ $W \cdot m^{-2} \cdot K^{-1}$) for the physical characterization of the collector.

Future work will focus on validating the model using long time sequences. The validated model will be used to simulate various scenarios for hydraulic configuration and control strategies. The objective of this approach is to optimize the solar contribution

5. Acknowledgement

This work was funded through a CIFRE fellowship in France, jointly by ANRT and FENGTECH. This research also benefited from the experimental installations previously implemented by the ICARE4FARMS project, funded by the INTERREG North West Europe program.

6. References

AEE - INTEC, 2025. Solar Heat Worldwide - Global Market Development and Trends 2024 - Detailed Market Figures 2023. https://doi.org/10.18777/ieashc-shww-2025-0001

Ahmadreza Mohammadkarim, Alibakhsh Kasaeian, Abdolrazagh Kaabinejadian, 2014. Performance Investigation of Solar Evacuated Tube Collector Using TRNSYS in Tehran.

Ayompe, L.M., Duffy, A., Mc Keever, M., Conlon, M., McCormack, S.J., 2011. Comparative field performance study of flat plate and heat pipe evacuated tube collectors (ETCs) for domestic water heating systems in a temperate climate. Energy 36, 3370–3378. https://doi.org/10.1016/j.energy.2011.03.034

Blank, J., Deb, K., 2020. Pymoo: Multi-Objective Optimization in Python. IEEE Access 8, 89497–89509. https://doi.org/10.1109/ACCESS.2020.2990567

Budihardjo, I., Morrison, G.L., 2009. Performance of water-in-glass evacuated tube solar water heaters. Sol. Energy 83, 49–56. https://doi.org/10.1016/j.solener.2008.06.010

Budihardjo, I., Morrison, G.L., Behnia, M., 2007. Natural circulation flow through water-in-glass evacuated tube solar collectors. Sol. Energy 81, 1460–1472. https://doi.org/10.1016/j.solener.2007.03.002

Chamsa-ard, W., Sukchai, S., Sonsaree, S., Sirisamphanwong, C., 2014. Thermal Performance Testing of Heat Pipe Evacuated Tube with Compound Parabolic Concentrating Solar Collector by ISO 9806 - 1. Energy Procedia 56, 237–246. https://doi.org/10.1016/j.egypro.2014.07.154

Cody Unrau, 2017. Numerical Investigation of One-Dimensional Storage Tank Models and the Development of Analytical Modelling Techniques.

Dileep, K., Raj, A., Dishnu, D., Saleel, A., Srinivas, M., Jayaraj, S., 2020. Computational fluid dynamics analysis on solar water heater: Role of thermal stratification and mixing on dynamic mode of operation. Therm. Sci. 24, 1461–1472. https://doi.org/10.2298/TSCI190601419D

Gambade, J., Noël, H., Glouannec, P., Magueresse, A., 2023. Numerical model of intermittent solar hot water production. Renew. Energy 218, 119368. https://doi.org/10.1016/j.renene.2023.119368

Garcia Sanchez, D., Lacarrière, B., Musy, M., Bourges, B., 2014. Application of sensitivity analysis in building energy simulations: Combining first- and second-order elementary effects methods. Energy Build. 68, 741–750. https://doi.org/10.1016/j.enbuild.2012.08.048

Ghaderian, J., Sidik, N.A.C., Kasaeian, A., Ghaderian, S., Okhovat, A., Pakzadeh, A., Samion, S., Yahya, W.J.,

2017. Performance of copper oxide/distilled water nanofluid in evacuated tube solar collector (ETSC) water heater with internal coil under thermosyphon system circulations. Appl. Therm. Eng. 121, 520–536. https://doi.org/10.1016/j.applthermaleng.2017.04.117

Gueymard, C.A., 2017. Cloud and albedo enhancement impacts on solar irradiance using high-frequency measurements from thermopile and photodiode radiometers. Part 1: Impacts on global horizontal irradiance. Sol. Energy 153, 755–765. https://doi.org/10.1016/j.solener.2017.05.004

Hayek, M., Assaf, J., Lteif, W., 2011. Experimental Investigation of the Performance of Evacuated-Tube Solar Collectors under Eastern Mediterranean Climatic Conditions. Energy Procedia 6, 618–626. https://doi.org/10.1016/j.egypro.2011.05.071

Herman, J., Usher, W., 2017. SALib: An open-source Python library for Sensitivity Analysis. J. Open Source Softw. 2, 97. https://doi.org/10.21105/joss.00097

ISO, 2025. ISO 9806:2025 Solar energy — Solar thermal collectors — Test methods.

Koffi, P.M.E., Andoh, H.Y., Gbaha, P., Touré, S., Ado, G., 2008. Theoretical and experimental study of solar water heater with internal exchanger using thermosiphon system. Energy Convers. Manag. 49, 2279–2290. https://doi.org/10.1016/j.enconman.2008.01.032

Morrison, G., Budihardjo, I., Behnia, M., 2004. Water-in-glass evacuated tube solar water heaters. Sol. Energy 76, 135–140. https://doi.org/10.1016/j.solener.2003.07.024

N'Tsoukpoe, K.E., Lekombo, C.S., Zorom, M., N'Tsoukpoe, K.G.J., Kuznik, F., 2026. Field survey insights and performance assessment of water-in-glass evacuated tube solar water heaters in Burkina Faso. Sci. Rep. 16, 17060. https://doi.org/10.1038/s41598-026-48447-w

Powell, M.J.D., 1964. An efficient method for finding the minimum of a function of several variables without calculating derivatives. Comput. J. 7, 155–162. https://doi.org/10.1093/comjnl/7.2.155

Rahimi-Ahar, Z., Khiadani, M., Rahimi Ahar, L., Shafieian, A., 2023. Performance evaluation of single stand and hybrid solar water heaters: a comprehensive review. Clean Technol. Environ. Policy 25, 2157–2184. https://doi.org/10.1007/s10098-023-02556-6

Sadeghi, G., Najafzadeh, M., Ameri, M., 2020. Thermal characteristics of evacuated tube solar collectors with coil inside: An experimental study and evolutionary algorithms. Renew. Energy 151, 575–588. https://doi.org/10.1016/j.renene.2019.11.050

Saltelli, A., 2002. Making best use of model evaluations to compute sensitivity indices. Comput. Phys. Commun. 145, 280–297. https://doi.org/10.1016/S0010-4655(02)00280-1

Singh, P., Gaur, M.K., Tiwari, G.N., Kumar, A., 2023. Thermal Modeling of Water-in-Tube Type Evacuated Tube Solar Collectors to Predict Outlet Water Temperature: An Experimental Validation. J. Sol. Energy Eng. 145, 021004. https://doi.org/10.1115/1.4055075

Siuta-Olcha, A., Cholewa, T., Dopieralska-Howoruszko, K., 2021. Experimental studies of thermal performance of an evacuated tube heat pipe solar collector in Polish climatic conditions. Environ. Sci. Pollut. Res. 28, 14319–14328. https://doi.org/10.1007/s11356-020-07920-3

Smyth, M., Eames, P.C., Norton, B., 2006. Integrated collector storage solar water heaters. Renew. Sustain. Energy Rev. 10, 503–538. https://doi.org/10.1016/j.rser.2004.11.001

Tang, R., Yang, Y., 2014. Nocturnal reverse flow in water-in-glass evacuated tube solar water heaters. Energy Convers. Manag. 80, 173–177. https://doi.org/10.1016/j.enconman.2014.01.025

Yang, X., Ji, Y., Gu, J., Niu, M., 2023. An Electricity Consumption Disaggregation Method for HVAC Terminal Units in Sub-Metered Buildings Based on CART Algorithm. Buildings 13, 967. https://doi.org/10.3390/buildings13040967

Zambolin, E., Del Col, D., 2010. Experimental analysis of thermal performance of flat plate and evacuated tube solar collectors in stationary standard and daily conditions. Sol. Energy 84, 1382–1396. https://doi.org/10.1016/j.solener.2010.04.020